

Strong Effects of Interlayer Interaction on Valence-Band Splitting in Transition Metal Dichalcogenides

Garrett Benson¹, Viviane Zurdo Costa¹, Neal Border¹, Kentaro Yumigeta², Mark Blei², Sefaattin Tongay², K. Watanabe,³ T. Taniguchi,³ Andrew Ichimura⁴, Santosh KC⁵, Taha Salavati-fard,⁶ Bin Wang,⁶ and Akm Newaz¹

¹Department of Physics and Astronomy, San Francisco State University, San Francisco, California 94132, USA

²School for Engineering of Matter, Transport and Energy, Arizona State University, Tempe, Arizona 85287, USA

³National Institute for Materials Science, Namiki 1-1, Tsukuba, Ibaraki 305-0044, Japan

⁴Department of Chemistry and Biochemistry, San Francisco State University, San Francisco, California 94132, USA

⁵Chemical and Materials Engineering, San Jose State University, San Jose, California 95112, USA

⁶School of Chemical, Biological and Materials Engineering, University of Oklahoma, Norman, Oklahoma 73019, United States

Date (December 8th, 2021)

Abstract

Understanding the origin of valence band maxima (VBM) splitting in transition metal dichalcogenides (TMDs) is important because it governs the unique spin and valley physics in monolayer and multilayer TMDs. In this work, we present our systematic study of VBM splitting (Δ) in atomically thin MoS₂ and WS₂ by employing photocurrent spectroscopy as we change the temperature and the layer numbers. We found that VBM splitting in monolayer MoS₂ and WS₂ depends strongly on temperature, which contradicts the theory that spin-orbit coupling solely determines the VBM splitting in monolayer TMDs. We also found that the rate of change of VBM splitting with respect to temperature ($m = \frac{\partial \Delta}{\partial T}$) is the highest for monolayer (-0.14 meV/K for MoS₂) and the rate decreases as the layer number increases ($m \sim 0$ meV/K for 5 layers MoS₂). We performed density functional theory (DFT) and the GW with Bethe-Salpeter Equation (GW-BSE) calculations to determine the electronic band structure and optical absorption for a bilayer MoS₂ with different interlayer separations. Our simulations agree with the experimental observations and demonstrate that the temperature dependence of VBM splitting in atomically thin monolayer and multilayer TMDs originates from the changes in the interlayer coupling strength between the neighboring layers. By studying two different types of TMDs and many different layer thicknesses, we also demonstrate that VBM splitting also depends on the layer numbers and type of transition metals. Our study will help understand the role spin-orbit coupling and interlayer interaction play in determining the VBM splitting in quantum materials and develop next-generation devices based on spin-orbit interactions.

Transition metal dichalcogenides (TMDs) exhibit remarkable properties resulting from their reduced dimensionality and crystal symmetry.¹⁻⁶ Monolayer TMDs (1L-TMDs) have a direct bandgap at the K point of the Brillouin zone, which is different from its corresponding few-layer and bulk counterparts with indirect band gaps.¹⁻⁶ The valence band maxima (VBM) at K point in TMDs split, which is attributed to the large spin-orbit coupling (SOC) in 1L-TMDs and the mixing of SOC and interlayer coupling for multilayer TMDs.⁷⁻¹³ Strong SOC in TMDs originate from the *d* –orbitals of the heavy transition-metal atoms.⁷ Unique crystal symmetry of TMDs causes coupling of spin and valley degrees of freedom.¹⁴ The crystal symmetry of TMDs and SOC cause a sizable split ($\Delta > 100$ meV) in the valence band at the K point in the Brillouin Zone (BZ). This large splitting governs many observable physical phenomena such as the spin-Hall effect,¹⁵ valley-Hall effect,¹⁶ and optical circular dichroism.¹⁷

Despite the importance of the VBM splitting that causes the unique spin and valley physics of TMDs, the temperature and layer dependence of VBM has not been well studied experimentally. In this work, we present our systematic study of VBM splitting in MoS₂ and WS₂ as we change the temperature and the layer number by employing photocurrent spectroscopy. Surprisingly, we have observed that the VBM in 1L-TMDs depends on the temperature, which contradicts the theory that VBM splitting in 1L-TMDs originates solely from the SOC. Our finding also contradicts two previously reported experimental study that concluded that the VBM splitting in monolayer originates from SOC only.^{13, 18} Intriguingly, we found that the temperature dependence is the strongest for 1L-MoS₂ than multilayer MoS₂. We also found that VBM in TMDs (MoS₂ and WS₂) also depends on the layer numbers and type of transition metals. We calculated the electronic band structure of bilayer MoS₂ by using density functional theory (DFT) and determined the absorption spectra using the GW-BSE approach, which agrees with experimentally measured VBM properties in MoS₂.

RESULTS AND DISCUSSION

To probe VBM splitting in atomically thin semiconductors, we have prepared molybdenum disulfide (MoS₂) and tungsten disulfide (WS₂) flakes that are electrically connected for transport measurement. All the samples reported here are covered by hexagonal boron nitride (hBN) for environmental protection. The MoS₂ and WS₂ flakes were mechanically exfoliated from bulk crystals onto a heavily doped silicon substrate capped with a 90 nm thick thermally grown SiO₂ film. The MoS₂ flakes were obtained from naturally grown rock and WS₂ samples were grown by chemical vapor transport (CVT) technique. The number of TMD layers was characterized by using optical microscopy, Raman spectroscopy, and atomic force microscopy (AFM).

For encapsulation with a few layers hBN, we prepare hBN flakes on SiO₂/Si substrate, which was picked by polyethylene terephthalate (PET). We used PET stamp to pick up the top hBN flake, atomically thin TMDs in sequence with accurate alignment using an optical microscope. The hBN/TMDs heterostructure was then stamped on a pre-fabricated Au electrode (70nm Au/ 5nm Cr) on a glass substrate (see Methods for details). The patterned Au electrodes were fabricated using optical lithography followed by thermal evaporation of metals. All devices were prepared on a glass substrate to avoid the photogating effect.¹⁹⁻²¹

Figure 1.a shows the optical images of a monolayer MoS₂ device encapsulated or covered by a hBN layer. The vertical design of the heterostructure sample is shown schematically in Fig.1a inset. Fig.1b shows the Raman spectrum for 1L, 2L, and 4L-MoS₂ samples. Confocal micro-Raman measurements were performed using commercial equipment (Horiba LabRAM 419 Evolution) (see Methods for details).

Reduced screening and strong light-matter interactions in van der Waals (vdWs) materials cause the formation of a wide range of many-body excitonic states. Intralayer excitons are bound electron-hole (*e-h*) pairs in the same layers, such as A-/B- excitons in TMDs originating from the split VBM at the K point. Hence, the measurement of A and B excitons provide a direct pathway to measure the VBM splitting. In addition to these many-body bound states, the band structure of 1L-TMDs causes a singularity in the joint density of states (JDoS) resulting in a unique exciton type, known as van Hove singularity excitons, also known as C and D excitons.^{19, 22}

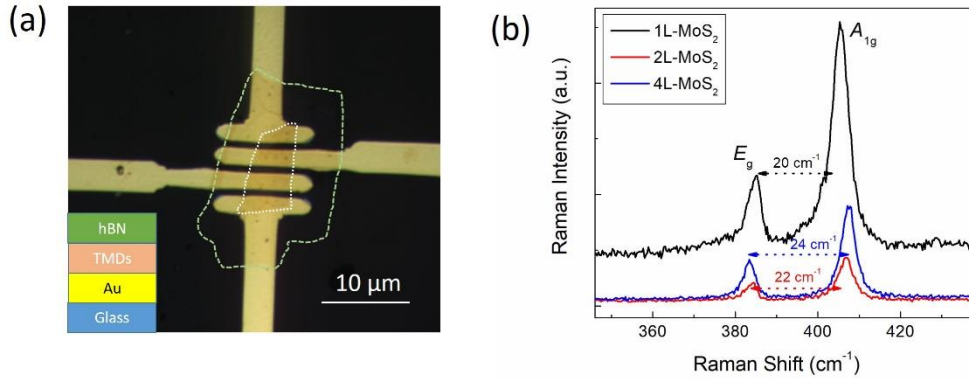


Figure 1: Left: Optical image of a 1L-MoS₂ sample connected to Au electrodes (yellow). The MoS₂ flake is marked by the dashed white line. The samples are covered by a few layer hBN flake marked by green dashed line. The left inset is showing the vertical structure of the sample schematically. Right: Raman spectrum of three different layer MoS₂ samples (monolayer, bilayer and 4-layers). The peak separation between E_g and A_{1g} are also shown. The excitation laser source was 532 nm.

To measure the VBM splitting directly, we have conducted photocurrent spectroscopy (PCS) at a varying temperature from 77K to 300 using a microscopy cryostat. We annealed every device using 532 nm high power laser (~200 mW) while the device was kept at 77 K inside the cryostat (see Methods for details). We illuminate devices using a low-intensity broadband white light from a thermal light source and record photocurrent generated from the device across a range of photon wavelengths (see Methods for details). In total, we studied 13 MoS₂ devices and 13 WS₂ devices (see Supporting Information for details).

Fig.2b presents the photocurrent spectroscopy for 1L- 5L MoS₂ samples measured at 77K. We observed clearly A, B, and C peaks in the spectrum as marked in Fig.2a. We also observed a small peak between B and C peaks, whose origin is not clear and beyond the scope of the paper. Further study is necessary to identify this new peak.

We present the photocurrent data in terms of photoresponsivity (i.e., the photocurrent generated per unit optical power). The sample was mounted inside a microscopy cryostat (Janis Research, ST-500) equipped with electrical feedthrough for electro-optical measurements. To collect the photocurrent, we biased the devices by different bias voltage ranging from 1V to 10V using a source-meter (Keithley 2400) (see Supporting Information for details).

Recently Zhang *et al.*,¹³ have demonstrated the temperature-dependent properties of VBM in MoS₂ by using photoluminescence (PL) spectroscopy. Though the reported results are interesting, we argue that their conclusions are heavily affected by two characteristics of PL measurements. First, the B peak in PL measurements is not prominent compared to the A-peak, which makes it challenging to pinpoint the B peak energy, which is critical to determine the VBM splitting. Second, PL is a second-order process where a TMD first absorb the photon exciting electrons to a conduction band from the valence band and then reemits a photon as the electron transitions to the valence band. On the other hand, PCS is a more precise technique to determine the SOC than PL spectroscopy as the PCS provide equally strong A and B peaks and the spectrums follow the absorption spectrums. We measured properties of VBM in TMDs that are significantly different than the results reported by Zhang *et al.*¹³ In particular, we have found strong temperature-dependent VBM in 1L- and 2L- TMDs, whereas Zhang *et al.* demonstrated temperature independent VBM for 1L- and 2L- MoS₂.

PC spectroscopy (PCS) is very similar to absorption spectroscopy and allows one to study single- and many-body electronic states, and valence band splitting in TMDs.¹⁹ Unlike absorption spectroscopy, PCS can be easily measured for an electrically contacted microscopic device in a cryogenic environment, as the device itself acts

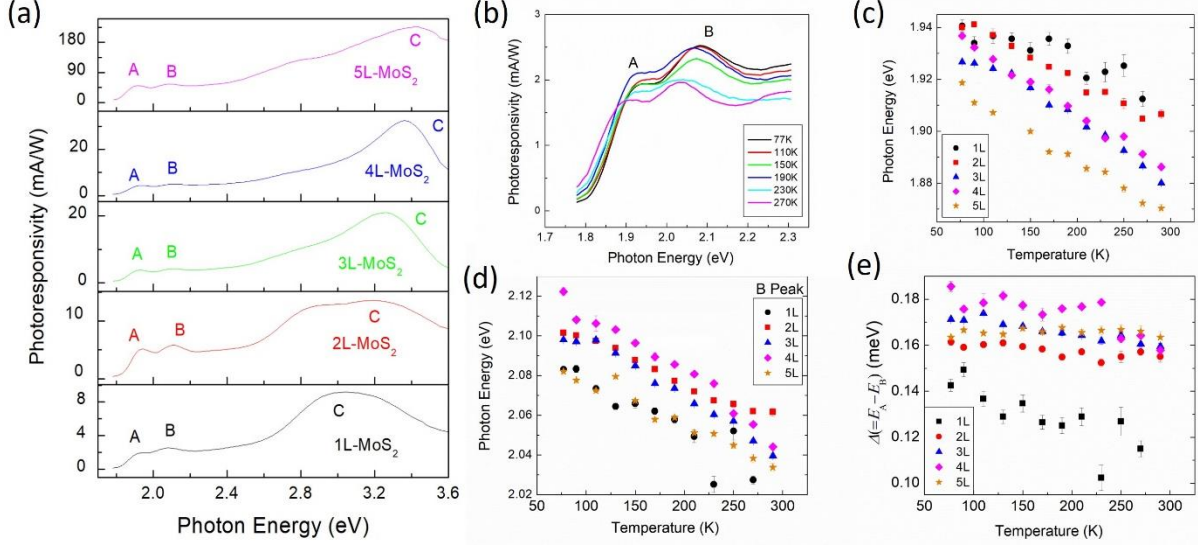


Figure 2: The VBM splitting of MoS₂. (a) Photocurrent spectra of different layered MoS₂ (1L to 5L). The left axis is presenting the photoresponsivity. (b) Photoresponsivity of a 1L-MoS₂ sample at different temperatures. (c) The plot is showing the A-peak position at different temperatures for different layered thickness. (d) The plot is showing the B-peak position at different temperatures for different layered thickness. (e) The difference between energy of the A and B peaks or VBM splitting Δ at different temperatures.

as its own photodetector. The peak separation in PCS of A and B peaks directly measures the VBM splitting in TMDs. We used Lorentzian fitting to determine the positions and errors of A and B peaks. Fig.2b presents the energy-resolved photoresponsivity spectrum at a different temperature ranging from 77 K to 270 K. We see that A and B peaks are red shifting as we increase the temperature. Fig.2c and 2d present the peak positions for the A and B peaks at different temperatures for different layered samples, respectively. We calculated VBM splitting from the difference between A and B peaks as shown in Fig.2e. The errors were calculated using the error propagation method.

The temperature-dependent VBM coupling strength for different layered flakes reveals three important features. First, we observed that VBM splitting in 1L-MoS₂ strongly depends on temperature. This is very surprising as the current theory indicates that VBM splitting in 1L-TMDs originates from the spin-orbit coupling only, which should be temperature-independent as SOC is a relativistic effect. Second, the rate of change of the coupling strength ($m = \frac{\partial \Delta}{\partial T}$) depends on the layer thickness. It is the highest for a monolayer MoS₂ (-0.14 meV/K) and it reduces to vanishingly small for 5L-MoS₂. Interestingly, we found that the rate becomes positive (0.08 meV/K) for bulk (~100 layers) MoS₂. Third, the VBM splitting value is lowest for monolayer and increases as we increase the layer thickness.

To understand the effect of the transition-metal ions in VBM splitting, we also studied SOC coupling in WS₂ by using photocurrent spectroscopy at varying temperatures and layer numbers. We have studied samples of different thicknesses ranging from monolayer (1L) to five layers (5L). Fig.3a presents the photocurrent spectroscopy data recorded at 77K for 1L-5L samples.

Fig.3b shows the photocurrent spectra at different temperatures for a bilayer WS₂ sample. Interestingly, the photoresponsivity increases as we increase the temperatures. We attribute this effect to the reduction of resistance of the devices. Fig.3c and 3d present the peak positions of A and B peak at different temperatures,

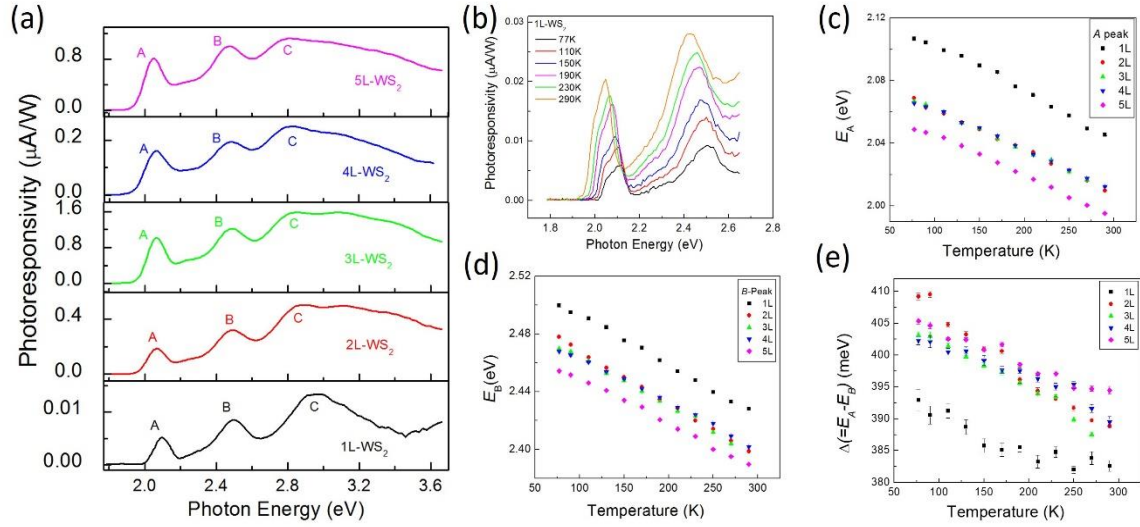


Figure 3: The VBM splitting of WS₂. (a) Photocurrent spectra of different layered WS₂ (1L to 5L). The left axis is presenting the photoresponsivity. (b) Photoresponsivity of a 1L-WS₂ sample at different temperatures. (c) The plot is showing the A-peak position at different temperatures for different layered thickness. (d) The plot is showing the B-peak position at different temperatures for different layered thickness. (e) The difference between energy of the A and B peaks, or VBM splitting Δ at different temperature for different thickness from 1L to 5L.

respectively. The peak positions and the corresponding errors were determined by fitting the Lorentzian function. Fig.3e presents the SOC coupling at different temperatures.

We observed 3 interesting features in the VBM splitting-temperature plots. First, VBM splitting, Δ , reduces as we increase the temperature. The reduction of Δ in 1L-WS₂ confirms that the splitting is not originating solely from SOC in a 1L-WS₂ similar to the case in 1L-MoS₂ as shown in Fig.3. Second, the rate of change Δ with respect to temperatures remain independent of layer thickness, which different than the trend observed for MoS₂. Finally, the VBM splitting in monolayer WS₂ is the lowest and it increases for multilayer WS₂.

To quantify the temperature-dependent change of VBM, we calculated the rate of change $m = \frac{\partial \Delta}{\partial T}$, for all the samples. We also studied a bulk MoS₂ sample (layer number ~ 100 determined by AFM thickness measurement) and a bulk WS₂ sample (layer number ~ 110). The calculated rate m for all the samples studied in this experiment is shown in Fig.4. It is evident from the plot that the rate m for MoS₂ increases as layer number increases up to 5L. Interestingly, we have not observed any clear trend for WS₂ samples depending on the layer thickness. For the bulk sample, m becomes positive for MoS₂, whereas m remains negative for WS₂. For two 10-layer MoS₂ samples, we observed widely separated m values, whose origin is not clear to us.

It has been argued that the splitting can be entirely attributed to SOC at the monolayer-limit,⁷⁻¹³ which suggests that the VBM splitting in 1L-TMDs should be independent of temperature. Instead, we observed the strongest temperature-dependent SOC for monolayer MoS₂ compared to a higher number of layers. Our result suggests that the VBM splitting at the monolayer limit is not solely due to SOC. We argue that the VBM splitting of 1L-MoS₂ originates from the mixing of SOC and the interlayer interaction with the substrate.

When a TMD is subjected to out-of-plane compressive pressure, it has been shown that the interlayer separation between adjacent TMD layer (δ) decreases and the interlayer interaction between the layer increases.^{18, 23} It has also been demonstrated that the Raman active vibrational modes (both E_g and A_{1g} modes)

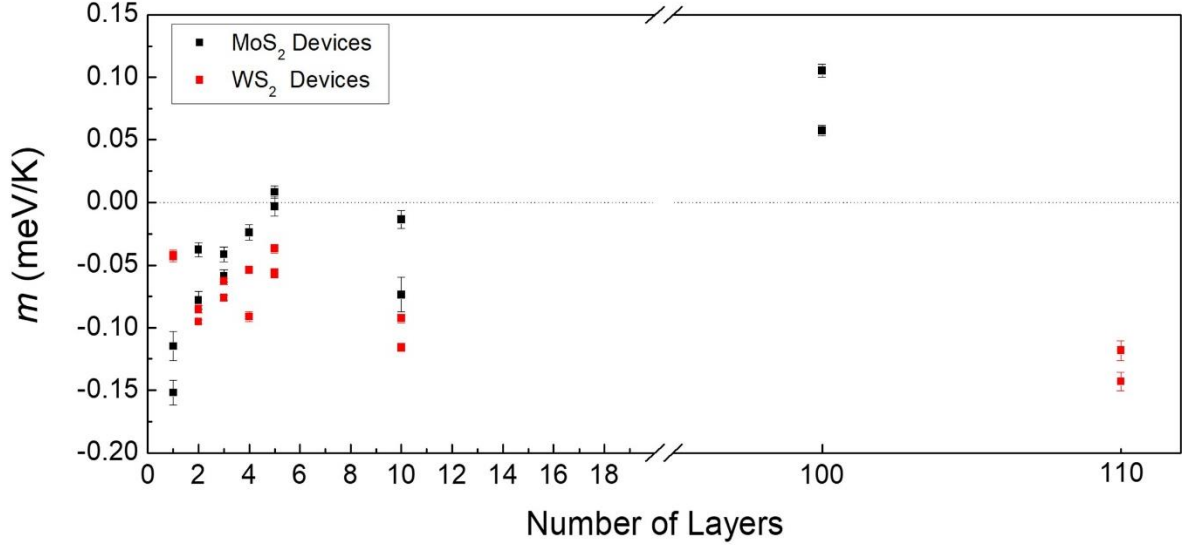


Figure 4: The rate ($m = \frac{\partial(E_A - E_B)}{\partial T}$) at which the splitting is behaving as we change the temperature for different layer MoS₂ and WS₂. To blow-up view of the splitting changing rate for 1L to 5L, a break in the x-axis is used. The error bars are also indicated.

blueshift as the pressure is increased,²⁴ which suggests that the blueshift (redshift) of the Raman peak is a signature of the decrease (increase) of interlayer separation δ and increase (decrease) of interlayer interaction. Since an increase in temperature causes a redshift of both E_g and A_{1g} Raman peaks,²⁵ the average interlayer separation δ increases, and interlayer interaction decreases as one increases the temperature. Hence, we argue that the observed temperature-dependence of VBM splitting in TMDs is originating from the change in the interlayer separation that affects the interlayer coupling strength.

To understand the effect of interlayer separation on VBM splitting, we conducted DFT and GW-BSE calculations to determine the band structure and absorption spectrums. In monolayer, there will be a combined effect of substrate dielectrics which is more pronounced in monolayer due to the reduced dimension and temperature effect. Moreover, the variability of the interface structure, effect of substrate strain, and dielectric screen effect with temperature is challenging and computational expensive that requires beyond DFT.^{26, 27} That is why we conducted calculations for only a bilayer MoS₂ at varying interlayer separation.

We simulated the electronic band structure using the DFT calculations. The calculations were performed using the Vienna *ab-initio* simulation package (VASP).^{28, 29} See Methods section for details. The electronic band structure calculated by DFT methods is shown in Fig.5(b), showing the VBM splitting at the K point of BZ.

To understand the excitonic A-B peak as a function of the interlayer separation of a bilayer MoS₂, we employ the GW-BSE method.³⁰ See Methods section for details. We observed from DFT calculations considering the relativistic effect that the VBM splitting is 155 meV in 2L MoS₂ for $d(S-S)=3.08$ Å. The calculated absorption spectra for three different values of $d(S-S) = 3.08$ Å, 3.33 Å, and 3.58 Å are shown in Fig.5(c). As we increase the interlayer separation, Δ (VBM) decreases as shown in Fig.5(d). To compare with the experimental observation, we have also re-plotted the Δ for a bilayer MoS₂ as shown in Fig.5(d).

Since we have measured Δ experimentally as a function of the temperature and calculated Δ as a function of interlayer separation, we can only make a qualitative comparison. Our results clearly demonstrate that the temperature dependence of Δ originates from the change in interlayer separation or interlayer interaction strengths. We have observed that Δ for a bilayer MoS₂ varies by ~ 10 meV as we change the temperature from

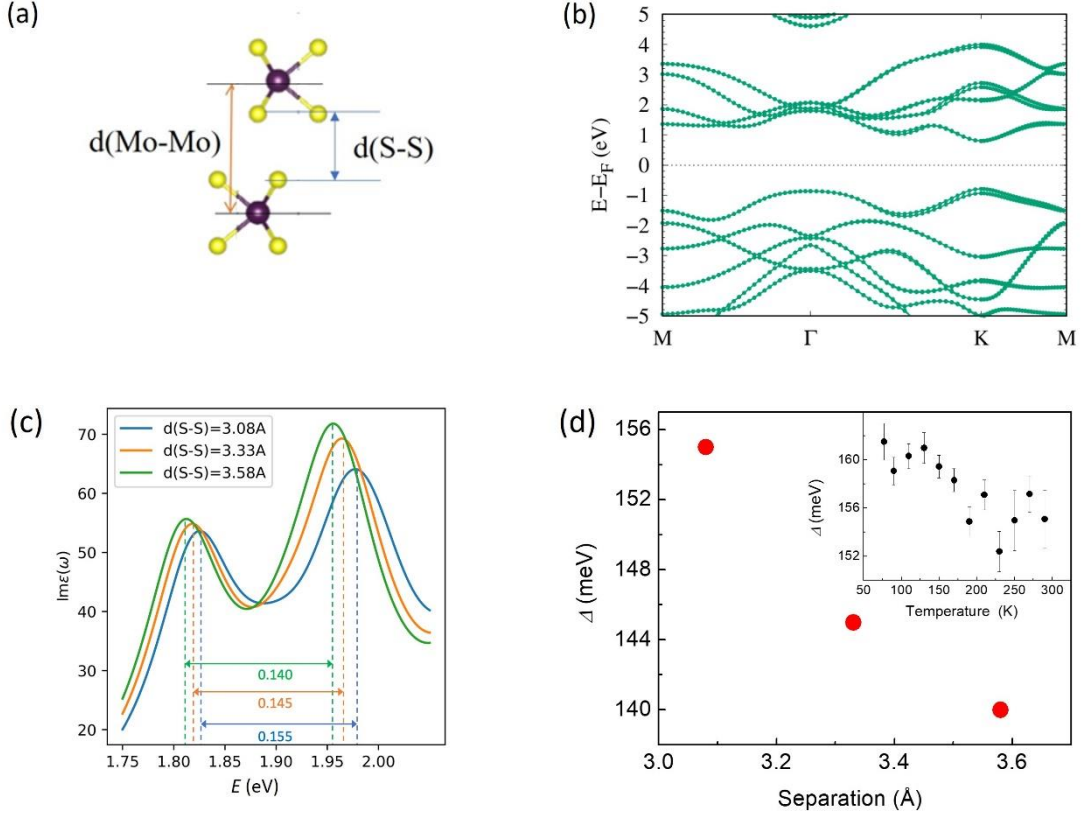


Figure 5: (a) Optimized atomic structure of a bilayer MoS₂. (b) Calculated electronic band structure with spin orbit coupling. (c) Absorption spectra for different interlayer $d(\text{S-S})$ separation for $d_0 = 3.08 \text{ \AA}$, $d_1 = 3.33 \text{ \AA}$, and $d_2 = 3.58 \text{ \AA}$. (d) Comparison of calculated VBM splitting values of a bilayer MoS₂ with the experimentally measured values. The main panel shows the calculated VBM splitting values for different interlayer separation. The inset is presenting experimentally measured VBM splitting for a 1L-MoS₂ as we change the temperature. The experimental results are the same data set presented in Fig.2(e).

77 K to 300 K. Interestingly, our simulation also predicts that the change in Δ very similar order as we increase the interlayer separation by 0.25 \AA . We note that there is a $\sim 10 \text{ meV}$ offset value between experimental measurements and simulations, but the trend still provides an explanation for the experimentally observed temperature-dependence of VBM splitting.

In conclusion, we studied temperature-, layer-, and material-dependent VBM for two different types of TMDs using photocurrent spectroscopy. We found that VBM depends on temperature, thickness, and materials of atomically thin TMDs. Our finding of VBM splitting in 1L-TMDs depending on temperature indicates that splitting Δ in 1L-TMDs does not originate solely from the SOC coupling. This result suggests that either SOC in 1L-TMDs is temperature-dependent or VBM splitting in 1L-TMDs is governed by the mixing of SOC and coupling strength to the substrate. Since SOC is a relativistic effect, we argue that VBM splitting in 1L-TMDs is caused by the mixing of SOC and the interaction with the substrate. We also found that the rate of change of SOC with respect to temperature is the highest for monolayer and the rate decreases as the layer number increases. To understand the effect, we have calculated the electronic band structure and VBM splitting for a bilayer with different interlayer separations, which suggests that the temperature-dependent VBM splitting in atomically 2L-TMDs can originate from the changes in the interlayer separation between neighboring layers.

Our study will help understand the intricate role spin-orbit coupling and interlayer interactions play in determining the VBM splitting in quantum materials.

Acknowledgment

G.B., V.Z.C., N. B., and A.K.M.N. acknowledge the support from the Department of Defense Award (ID: 72495RTREP). A.K.M.N. also acknowledges the support from the National Science Foundation Grant ECCS-1708907 and the faculty start-up grant provided by the College of Science and Engineering at San Francisco State University. S. KC acknowledges the faculty start-up grant provided by the Davidson College of Engineering at San Jose State University. Part of this research used resources of the National Energy Research Scientific Computing Center (NERSC), a U.S. Department of Energy Office of Science User Facility located at Lawrence Berkeley National Laboratory, operated under Contract No. DE-AC02-05CH11231 and Extreme Science and Engineering Discovery Environment (XSEDE), which is supported by National Science Foundation grant number ACI-1548562. T. S. and B. W. are supported by Basic Energy Sciences, Office of Science, Department of Energy (Grant No. DE-SC0020300). S.T acknowledges support from NSF CMMI-1933214, NSF DMR-2111812, CMMI-2129412, and NSF ECCS-2052527 as well as DOE-SC0020653. All AFM measurements were supported by NSF for instrumentation facilities (NSF MRI-CMMI 1626611). All Raman spectroscopy data were acquired at the Stanford Nano Shared Facilities (SNSF), supported by the National Science Foundation under award ECCS-2026822.

Methods:

Sample Fabrication: Atomically thin MoS₂ and WS₂ flakes were mechanically exfoliated from bulk crystals onto a heavily doped silicon substrate capped with a 90 nm thick thermal grown SiO₂ film. The MoS₂ flakes were obtained from naturally grown rock and WS₂ samples were grown by chemical vapor transport (CVT) technique. The number of TMD layers was characterized by using optical microscopy, Raman spectroscopy, and atomic force microscopy (AFM). For encapsulation with a few layers hBN, we prepare hBN flakes on SiO₂/Si substrate, which was picked by polyethylene terephthalate (PET). We used PET stamp to pick up the top hBN flake, atomically thin TMDs in sequence with accurate alignment using an optical microscope. The hBN/TMDs heterostructure was then stamped on a pre-fabricated Au electrode (70nm Au/ 5nm Cr) on a glass substrate. The patterned Au electrodes were fabricated using optical lithography followed by thermal evaporation of metals. All devices were prepared on a glass substrate to avoid the photogating effect.¹⁹⁻²¹

Raman Characterization: Confocal micro-Raman measurements were performed using commercial equipment (Horiba LabRAM Evolution). A 100× objective lens with a numerical aperture of 0.9 was used. The excitation source was a 532 nm laser (2.33 eV) with an optical power of ~170 μW.

Laser Assisted Thermal Annealing: To obtain lower contact resistance, we annealed the devices using a 532 nm laser of beam power ~200 mW. The beam diameter is ~ 2 μm. We kept the devices at 77 K and under a bias voltage while we annealed the devices. The bias voltages were varied depending on the devices to obtain a measurable current. After annealing for 2 minutes, we measure the photocurrent spectroscopy. If the signal to noise ratio in photocurrent is low we repeated the laser assisted annealing process. We continued the process until we obtain a high signal to low noise ratio.

Photocurrent Spectroscopy: The photocurrent spectroscopy (PCS) at a varying temperature from 77K to 300 was conducted using a microscopy cryostat (Janis Research). We illuminate devices using a low-intensity broadband white light from a thermal light source and record photocurrent generated from the device across a range of photon wavelengths. The optical beam from the broadband thermal source (quartz halogen lamp) was directed through a monochromator (Acton Pro SP-2150i) and a mechanical chopper (45 Hz) onto the sample where it was focused down to a spot (~10 μm) with a diameter larger than the device. The photocurrent was measured by using a preamplifier (SRS570) connected to a lock-in-amplifier (SRS-830), which was locked to the chopping frequency. A commercial silicon photodetector (Hamamatsu S1223) was used to calibrate the light intensity incident on the sample.

DFT calculations: The DFT calculations were performed using the Vienna *ab-initio* simulation package (VASP).^{28, 29} The nuclei and core electrons were described by the projector augmented wave function (PAW).^{31, 32} The exchange-correlation used was the generalized gradient approximation (GGA) of Perdew–Burke–Ernzerhof (PBE) functional. All the structures were optimized until the maximum Hellmann-Feynman forces acting on each atom and the total energy is less than 0.01 eV/Å and 10⁻⁵ eV, respectively. Each slab has a vacuum thickness of 20 Å along z-direction to avoid the interaction due to periodic boundary conditions.

We used the GW-BSE method to calculate the absorption spectrum of TMDs.³⁰ The GPAW electronic structure calculations software,^{33, 34} version 21.6.0, was employed to calculate the dielectric functions of the studied systems. Using the imaginary part of the dielectric function, optical adsorption spectrum and excitonic A and B peaks within the GW-BSE level of theory, which includes electron-hole correlations, were obtained. The reciprocal space was sampled by highly fine 30x30x1 k-points grid and truncated Coulomb interaction was considered to decouple the screening between periodic images.³⁵ The cut-off energy for the response function was set to 50 eV. The four highest energy bands below and the four lowest energy bands above the Fermi level were included in the GW-BSE calculations.

References:

1. Wang, Q. H.; Kalantar-Zadeh, K.; Kis, A.; Coleman, J. N.; Strano, M. S., Electronics and optoelectronics of two-dimensional transition metal dichalcogenides. *Nat Nano* **2012**, *7* (11), 699-712.
2. Mak, K. F.; Shan, J., Photonics and optoelectronics of 2D semiconductor transition metal dichalcogenides. *Nat Photon* **2016**, *10* (4), 216-226.
3. Xia, F.; Wang, H.; Xiao, D.; Dubey, M.; Ramasubramaniam, A., Two-dimensional material nanophotonics. *Nat Photon* **2014**, *8* (12), 899-907.
4. Duan, X.; Wang, C.; Pan, A.; Yu, R.; Duan, X., Two-dimensional transition metal dichalcogenides as atomically thin semiconductors: opportunities and challenges. *Chemical Society Reviews* **2015**, *44* (24), 8859-8876.
5. Jariwala, D.; Sangwan, V. K.; Lauhon, L. J.; Marks, T. J.; Hersam, M. C., Emerging Device Applications for Semiconducting Two-Dimensional Transition Metal Dichalcogenides. *ACS Nano* **2014**, *8* (2), 1102-1120.
6. Manzeli, S.; Ovchinnikov, D.; Pasquier, D.; Yazyev, O. V.; Kis, A., 2D transition metal dichalcogenides. *Nature Reviews Materials* **2017**, *2*, 17033.
7. Zhu, Z. Y.; Cheng, Y. C.; Schwingenschlögl, U., Giant spin-orbit-induced spin splitting in two-dimensional transition-metal dichalcogenide semiconductors. *Physical Review B* **2011**, *84* (15), 153402.
8. Sun, L.; Yan, J.; Zhan, D.; Liu, L.; Hu, H.; Li, H.; Tay, B. K.; Kuo, J.-L.; Huang, C.-C.; Hewak, D. W.; Lee, P. S.; Shen, Z. X., Spin-Orbit Splitting in Single-Layer MoS₂ Revealed by Triply Resonant Raman Scattering. *Physical Review Letters* **2013**, *111* (12), 126801.
9. Alidoust, N.; Bian, G.; Xu, S.-Y.; Sankar, R.; Neupane, M.; Liu, C.; Belopolski, I.; Qu, D.-X.; Denlinger, J. D.; Chou, F.-C.; Hasan, M. Z., Observation of monolayer valence band spin-orbit effect and induced quantum well states in MoX₂. *Nature Communications* **2014**, *5* (1), 4673.
10. Molina-Sanchez, A.; Sangalli, D.; Hummer, K.; Marini, A.; Wirtz, L., Effect of spin-orbit interaction on the optical spectra of single-layer, double-layer, and bulk MoS₂. *Physical Review B* **2013**, *88* (4), 045412.
11. Cheiwchanamngij, T.; Lambrecht, W. R. L., Quasiparticle band structure calculation of monolayer, bilayer, and bulk MoS₂. *Physical Review B* **2012**, *85* (20), 205302.
12. Latzke, D. W.; Zhang, W.; Suslu, A.; Chang, T.-R.; Lin, H.; Jeng, H.-T.; Tongay, S.; Wu, J.; Bansil, A.; Lanzara, A., Electronic structure, spin-orbit coupling, and interlayer interaction in bulk MoS₂ and WS₂. *Physical Review B* **2015**, *91* (23), 235202.
13. Zhang, Y.; Li, H.; Wang, H.; Liu, R.; Zhang, S.-L.; Qiu, Z.-J., On Valence-Band Splitting in Layered MoS₂. *ACS Nano* **2015**, *9* (8), 8514-8519.
14. Mak, K. F.; He, K.; Shan, J.; Heinz, T. F., Control of valley polarization in monolayer MoS₂ by optical helicity. *Nat Nano* **2012**, *7* (8), 494-498.
15. Bhowal, S.; Satpathy, S., Intrinsic orbital and spin Hall effects in monolayer transition metal dichalcogenides. *Physical Review B* **2020**, *102* (3), 035409.

16. Zhou, B. T.; Taguchi, K.; Kawaguchi, Y.; Tanaka, Y.; Law, K. T., Spin-orbit coupling induced valley Hall effects in transition-metal dichalcogenides. *Communications Physics* **2019**, *2* (1), 26.
17. Cao, T.; Wang, G.; Han, W.; Ye, H.; Zhu, C.; Shi, J.; Niu, Q.; Tan, P.; Wang, E.; Liu, B.; Feng, J., Valley-selective circular dichroism of monolayer molybdenum disulphide. *Nature Communications* **2012**, *3*, 887.
18. Dou, X.; Ding, K.; Jiang, D.; Fan, X.; Sun, B., Probing Spin–Orbit Coupling and Interlayer Coupling in Atomically Thin Molybdenum Disulfide Using Hydrostatic Pressure. *ACS Nano* **2016**, *10* (1), 1619-1624.
19. Klots, A. R.; Newaz, A. K. M.; Wang, B.; Prasai, D.; Krzyzanowska, H.; Lin, J.; Caudel, D.; Ghimire, N. J.; Yan, J.; Ivanov, B. L.; Velizhanin, K. A.; Burger, A.; Mandrus, D. G.; Tolk, N. H.; Pantelides, S. T.; Bolotin, K. I., Probing excitonic states in suspended two-dimensional semiconductors by photocurrent spectroscopy. *Sci. Rep.* **2014**, *4*, 6608.
20. Freitag, M.; Low, T.; Xia, F.; Avouris, P., Photoconductivity of biased graphene. *Nature Photonics* **2013**, *7* (1), 53-59.
21. Konstantatos, G.; Badioli, M.; Gaudreau, L.; Osmond, J.; Bernechea, M.; de Arquer, F. P. G.; Gatti, F.; Koppens, F. H. L., Hybrid graphene-quantum dot phototransistors with ultrahigh gain. *Nat Nano* **2012**, *7* (6), 363-368.
22. Qiu, D. Y.; da Jornada, F. H.; Louie, S. G., Optical Spectrum of MoS₂: Many-Body Effects and Diversity of Exciton States. *Physical Review Letters* **2013**, *111* (21), 216805.
23. Ci, P.; Chen, Y.; Kang, J.; Suzuki, R.; Choe, H. S.; Suh, J.; Ko, C.; Park, T.; Shen, K.; Iwasa, Y.; Tongay, S.; Ager, J. W.; Wang, L.-W.; Wu, J., Quantifying van der Waals Interactions in Layered Transition Metal Dichalcogenides from Pressure-Enhanced Valence Band Splitting. *Nano Letters* **2017**, *17* (8), 4982-4988.
24. Li, X.; Li, J.; Wang, K.; Wang, X.; Wang, S.; Chu, X.; Xu, M.; Fang, X.; Wei, Z.; Zhai, Y.; Zou, B., Pressure and temperature-dependent Raman spectra of MoS₂ film. *Applied Physics Letters* **2016**, *109* (24), 242101.
25. Sahoo, S.; Gaur, A. P. S.; Ahmadi, M.; Guinel, M. J. F.; Katiyar, R. S., Temperature-Dependent Raman Studies and Thermal Conductivity of Few-Layer MoS₂. *The Journal of Physical Chemistry C* **2013**, *117* (17), 9042-9047.
26. Ryou, J.; Kim, Y.-S.; Kc, S.; Cho, K., Monolayer MoS₂ Bandgap Modulation by Dielectric Environments and Tunable Bandgap Transistors. *Scientific Reports* **2016**, *6* (1), 29184.
27. Kc, S.; Longo, R. C.; Wallace, R. M.; Cho, K., Computational Study of MoS₂/HfO₂ Defective Interfaces for Nanometer-Scale Electronics. *ACS Omega* **2017**, *2* (6), 2827-2834.
28. Kresse, G.; Furthmüller, J., Efficient iterative schemes for ab initio total-energy calculations using a plane-wave basis set. *Physical Review B* **1996**, *54* (16), 11169-11186.
29. Kresse, G.; Furthmüller, J., Efficiency of ab-initio total energy calculations for metals and semiconductors using a plane-wave basis set. *Computational Materials Science* **1996**, *6* (1), 15-50.
30. Onida, G.; Reining, L.; Rubio, A., Electronic excitations: density-functional versus many-body Green's-function approaches. *Reviews of Modern Physics* **2002**, *74* (2), 601-659.
31. Blöchl, P. E., Projector augmented-wave method. *Physical Review B* **1994**, *50* (24), 17953-17979.
32. Perdew, J. P.; Burke, K.; Ernzerhof, M., Generalized Gradient Approximation Made Simple. *Physical Review Letters* **1996**, *77* (18), 3865-3868.
33. Mortensen, J. J.; Hansen, L. B.; Jacobsen, K. W., Real-space grid implementation of the projector augmented wave method. *Physical Review B* **2005**, *71* (3), 035109.
34. Enkovaara, J.; Rostgaard, C.; Mortensen, J. J.; Chen, J.; Dulak, M.; Ferrighi, L.; Gavnholt, J.; Glinsvad, C.; Haikola, V.; Hansen, H. A.; Kristoffersen, H. H.; Kuisma, M.; Larsen, A. H.; Lehtovaara, L.; Ljungberg, M.; Lopez-Acevedo, O.; Moses, P. G.; Ojanen, J.; Olsen, T.; Petzold, V.; Romero, N. A.; Stausholm-Møller, J.; Strange, M.; Tritsarlis, G. A.; Vanin, M.; Walter, M.; Hammer, B.; Häkkinen, H.; Madsen, G. K. H.; Nieminen, R. M.; Nørskov, J. K.; Puska, M.; Rantala, T. T.; Schiøtz, J.; Thygesen, K. S.; Jacobsen, K. W., Electronic structure calculations with GPAW: a real-space implementation of the projector augmented-wave method. *Journal of Physics: Condensed Matter* **2010**, *22* (25), 253202.
35. Huser, F.; Olsen, T.; Thygesen, K. S., How dielectric screening in two-dimensional crystals affects the convergence of excited-state calculations: Monolayer MoS₂. *Physical Review B* **2013**, *88* (24), 245309.

Supporting Information

Strong Effects of Interlayer Interaction on Valence-Band Splitting in Transition Metal Dichalcogenides

Garrett Benson¹, Viviane Zurdo Costa¹, Neal Border¹, Kentaro Yumigeta², Mark Blei², Sefaattin Tongay², K. Watanabe,³ T. Taniguchi,³ Andrew Ichimura⁴, Santosh KC⁵, Taha Salavati-fard,⁶ Bin Wang,⁶ and Akm Newaz¹

¹Department of Physics and Astronomy, San Francisco State University, San Francisco, California 94132, USA

² School for Engineering of Matter, Transport and Energy, Arizona State University, Tempe, Arizona 85287, United States;

³ National Institute for Materials Science, Namiki 1-1, Tsukuba, Ibaraki 305-0044, Japan

⁴Department of Chemistry and Biochemistry, San Francisco State University, San Francisco, California 94132, USA

⁵Chemical and Materials Engineering, San Jose State University, San Jose, California 95112, USA

⁶School of Chemical, Biological and Materials Engineering, University of Oklahoma, Norman, Oklahoma 73019, United States

1) Pre-patterned Au electrodes Fabrication

To fabricate Au electrodes, we have selected are alkaline earth boro-aluminosilicate glasses obtained from Delta Technologies (C-1737). The glass thickness was 0.7 mm. The substrates were rinsed with copious deionized water, dried under argon, and then coated with positive photoresist (Microposit 1818). We have used 400 RPM spin coat rate to prepare a uniform photoresist film. After optical lithography, the wafer was transferred to a bell jar. We evacuated the bell jar to a base pressure of 10^{-7} Torr followed by a deposition Cr (5nm)/Au (100 nm) at a rate of 5 \AA/s . Metal lift-off was conducted using an ultra-sonicator instrument. The fabrication process is shown in Fig.S1

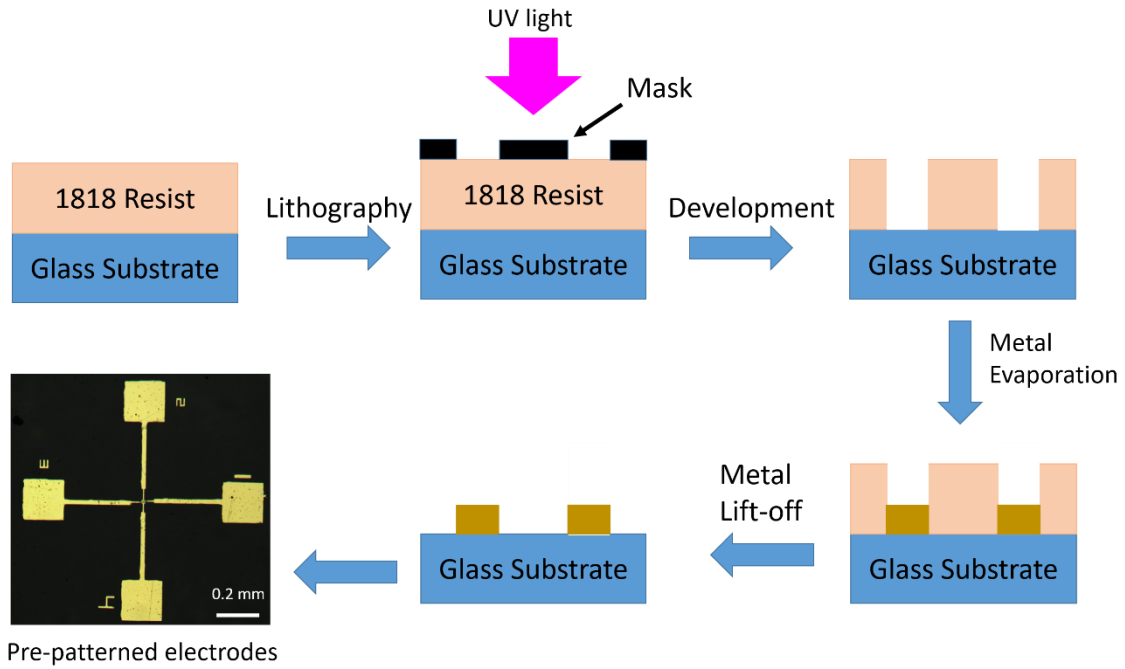


Figure S1: The fabrication process of the pre-patterned Cr/Au electrodes on a glass substrate. The optical image of a final fabricated electrodes on a boro-silicate glass is shown in the bottom left. The large metal squares ($200 \mu\text{m} \times 200 \mu\text{m}$) shown in the optical image are used for the wire bonding.

2) Monolayer WS₂ sample characterization

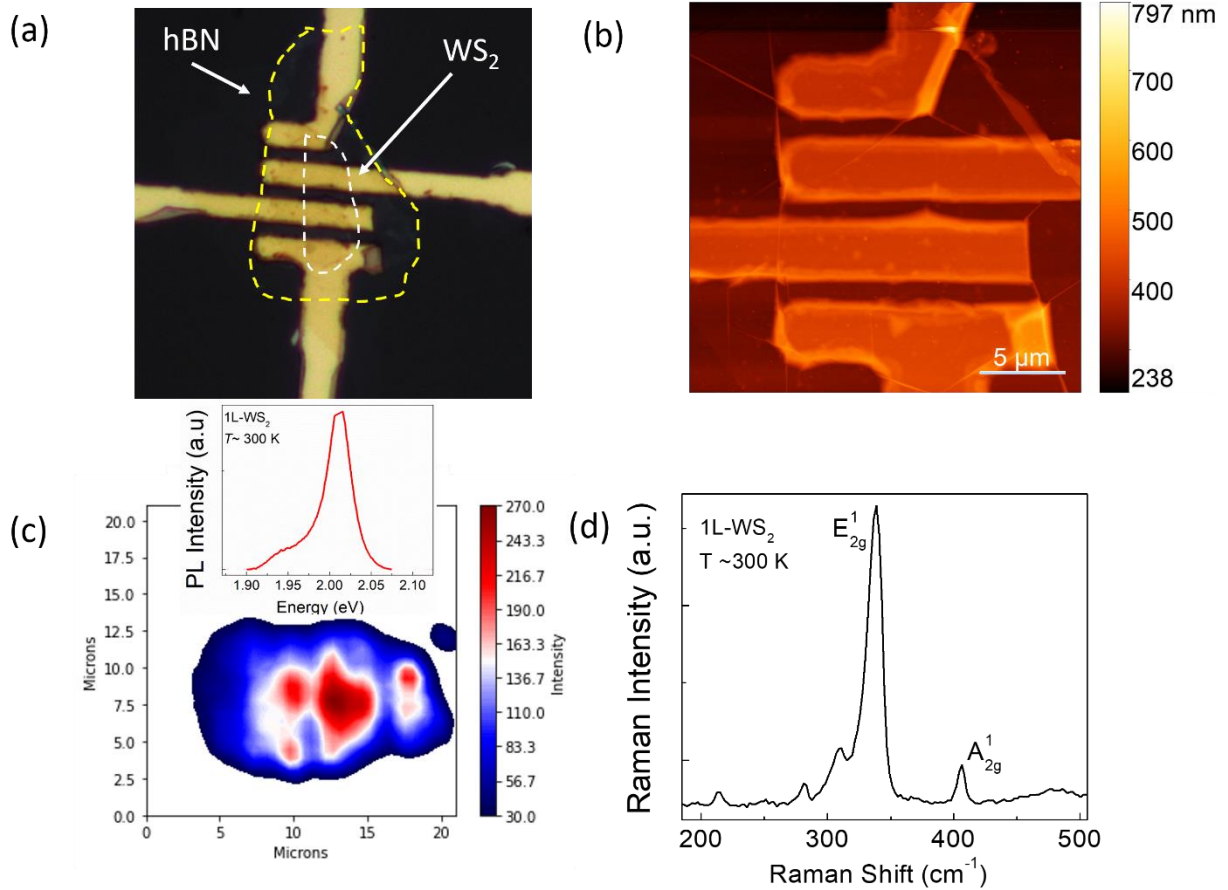


Figure S2: (a) Optical image of a 1L-WS₂ sample connected to Au electrodes (yellow). The WS₂ flake is marked by the dashed white line. The samples are covered by a few layer hBN flake marked by yellow dashed line. (b) An AFM image of the same sample. (c) The photoluminescence mapping of the sample at room temperature. This is a spatial contour plot showing the integrated PL intensity for different location of the laser beam on the sample. The inset presents the PL spectrum from the sample measured at room temperature. The laser excitation wavelength was 532 nm. (d) The Raman spectrum from the sample recorded at room temperature. The wavelength of the laser excitation was 532 nm.

3) Device information:

The table below presents the device information for MoS₂ and WS₂ samples.

Device No.	Layer(s)	Bias Voltage (V)	PC Spectral Range (nm)	hBN
9A	1	6	540-700	Yes
9C	1	8	300-700	Yes
1B	2	2	300-700	Yes
11C	2	4	300-700	Yes
13A	3	4	540-700	Yes
13B	3	3	340-700	Yes
5B	4	2	300-700	Yes
15A	5	3	340-700	Yes
15B	5	1	540-700	Yes
27A	10	4	580-680	Yes
27B	10	3	340-700	Yes
17B	Bulk	10	340-700	No
17C	Bulk	10	340-700	No

Table 1: Information of MoS₂ devices. The second column presents the layer number. The bulk is used for devices that are ~100 layer thick. The third column presents the bias voltages used for photocurrent measurement. The fourth column presents the spectra range used for photocurrent measurement. The fifth column presents whether we cover the device the with atomically thin hBN flake.

Device No.	Layer(s)	Bias Voltage (V)	PC Spectral Range (nm)	hBN
33B	1	1	340-700	Yes
33C	1	1	340-700	Yes
18B	2	6	540-700	Yes
18C	2	8	300-700	Yes
23B	3	2	300-700	Yes
23C	3	4	300-700	Yes
21A	4	4	540-700	Yes
21C	4	2	300-700	Yes
22A	5	3	340-700	Yes
22B	5	1	540-700	Yes
22C	5	4	580-680	Yes
28A	Bulk	3	340-700	Yes
28B	Bulk	10	340-700	No

Table 1: Information of WS₂ devices. The second column presents the layer number. The bulk is used for devices that are ~100 layer thick. The third column presents the bias voltages used for photocurrent measurement. The fourth column presents the spectra range used for photocurrent measurement. The fifth column presents whether we cover the device the with atomically thin hBN flake.